Behavior of rigid and deformable particles in deterministic lateral displacement devices with different post shapes

Zunmin Zhang, Ewan Henry, Gerhard Gompper, and Dmitry A. Fedosov

Citation: The Journal of Chemical Physics **143**, 243145 (2015); doi: 10.1063/1.4937171
View online: http://dx.doi.org/10.1063/1.4937171
View Table of Contents: http://scitation.aip.org/content/aip/journal/jcp/143/24?ver=pdfcov
Published by the AIP Publishing

Behavior of rigid and deformable particles in deterministic lateral displacement devices with different post shapes

Zunmin Zhang, Ewan Henry, Gerhard Gompper, and Dmitry A. Fedosov[a)]
Theoretical Soft Matter and Biophysics, Institute of Complex Systems and Institute for Advanced Simulation, Forschungszentrum Jülich, 52425 Jülich, Germany

(Received 20 September 2015; accepted 23 November 2015; published online 14 December 2015)

Deterministic lateral displacement (DLD) devices have great potential for the separation and sorting of various suspended particles based on their size, shape, deformability, and other intrinsic properties. Currently, the basic idea for the separation mechanism is that the structure and geometry of DLDs uniquely determine the flow field, which in turn defines a critical particle size and the particle lateral displacement within a device. We employ numerical simulations using coarse-grained mesoscopic methods and two-dimensional models to elucidate the dynamics of both rigid spherical particles and deformable red blood cells (RBCs) in different DLD geometries. Several shapes of pillars, including circular, diamond, square, and triangular structures, and a few particle sizes are considered. The simulation results show that a critical particle size can be well defined for rigid spherical particles and depends on the details of the DLD structure and the corresponding flow field within the device. However, non-isotropic and deformable particles such as RBCs exhibit much more complex dynamics within a DLD device, which cannot properly be described by a single parameter such as the critical size. The dynamics and deformation of soft particles within a DLD device become also important, indicating that not only size sorting, but additional sorting targets (e.g., shape, deformability, internal viscosity) are possible. © *2015 AIP Publishing LLC.* [http://dx.doi.org/10.1063/1.4937171]

I. INTRODUCTION

The deterministic lateral displacement (DLD) approach[1] for particle and cell sorting has attracted considerable research and technological interest for developing novel microfluidic devices for biological and clinical applications. Starting from its invention by Huang *et al.*[2] as a size-dependent (label-free) particle-separation method, this technique has been continuously used and developed further. DLD devices are now able to separate multiple particles with an extremely high resolution of about 20 nm when applied to the sorting of polystyrene beads.[2–4] Other applications also include the separation of parasites from human blood,[5] fractionation of human blood cells,[6,7] and sorting of droplets in microfluidics.[8] This demonstrates a great potential of DLDs for the separation and detection of various rigid and deformable particles in a suspension based on particle properties such as size, shape, deformability, and potentially other intrinsic characteristics. However, a rational design of such devices requires a detailed understanding of the flow behavior of different particles in complex geometrical DLD structures.

In general, a DLD device consists of a row-shifted array of micron-sized pillars (or posts) residing in the flow channel. As shown in Fig. 1, the posts are arranged in different rows and each row is shifted laterally with respect to the previous one. The geometry and arrangement of posts (e.g., post shape, post gap G, row shift $\Delta\lambda$) determine a critical particle size D_c for the DLD device. According to the theory,[2] particles smaller than D_c tend to move in the direction of flow known as "zigzag mode," whereas particles larger than D_c are laterally displaced and move along the post array gradient known as "displacement mode." In this way, different particles can be separated by collecting them at different outlets of a DLD device and thus, the knowledge about critical size allows the design of devices for sorting specific sizes of rigid spherical particles. Recently, a third motion named "mixed mode" has been observed in experiments and simulations,[9,10] which shows an irregular alternation of zigzag and displacement modes. The erratic nature of the mixed mode may smear the otherwise deterministic nature of a DLD device and consequently complicate device design and application.

The deterministic separation mechanism described above functions well for rigid spherical particles whose sizes remain constant under various experimental conditions (e.g., flow rate). In practice, it is desirable to separate more exotic particles with different rigidities and shapes; for instance, red blood cells (RBCs) are soft and non-spherical. Particles with various rigidities will deform to a different extent under the shear forces experienced in flow. Examples include vesicles in structured microchannels,[11] RBCs in cylindrical vessels,[12–15] and synthetic microcapsules in shear flow.[16–18] Thus, the effective size of soft particles will vary depending on their location in the complex flow field within the post array. Furthermore, particles with non-isotropic shapes have varying effective size depending on their orientation relative to the post array. For example, Beech *et al.*[19] have presented an orientation- and deformation-based separation of RBCs achieved by the reduction of the channel depth and the change of flow rate within the device, respectively. These two uncertainties in

[a)]Author to whom correspondence should be addressed. Electronic mail: d.fedosov@fz-juelich.de

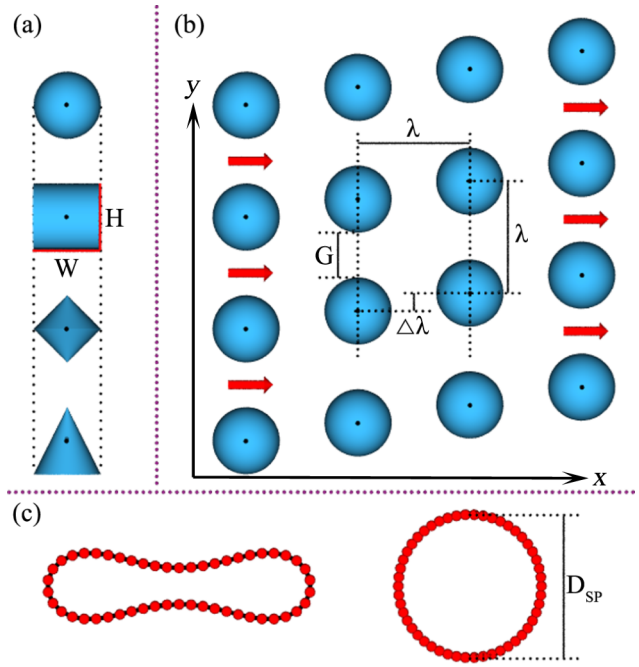

FIG. 1. Schematic illustration of the geometry and structures of simulated DLD systems. (a) Typical post shapes (circle, square, diamond, and triangle) with $W = H = 15$ μm. (b) DLD array with circular posts. The geometry is defined by the post center-to-center distance $\lambda = 25$ μm, the post gap $G = 10$ μm, and the row shift $\Delta\lambda$. The red arrows indicate the direction of flow. (c) 2D models of RBCs and rigid circular particles.

effective size do not necessarily destroy the determinism of a DLD device, but they certainly make it harder to predict which mode of motion a particle will adopt in transit through a DLD device. In addition, there is no clear evidence that conventional circular post arrays are the best option, which makes the geometry of posts an important additional parameter to explore. Zeming *et al.*[20] have created a DLD device with I-shaped posts in order to induce RBC rotation, which consequently increases the hydrodynamic size of RBCs and alters their behavior within the DLD device. Al-Fandi *et al.*[21] have proposed airfoil-like and diamond-like post shapes and found that the airfoil post array appears to be better for the reduction of clogging and deformation of soft particles. Loutherback *et al.*[3,4] have demonstrated that the use of a triangular post array can significantly enhance the performance of DLD devices by reducing their clogging, lowering hydrostatic pressure requirements, and increasing the range of displacement-type dynamics. In view of these studies, post shape plays an important role in controlling the separation effectiveness of various particles by modifying the flow profiles within DLD arrays and introducing novel particle trajectories.

Attempting to experimentally realize the transit modes for the myriad of combinations of particle shapes and properties, device geometries, and post shapes would be very expensive and extremely time-consuming. Simulations provide a valuable alternative, allowing systematic exploration of particle transit behavior through novel post-array geometries. Several numerical simulations[22–24] have investigated the behavior of elastic capsules and RBCs in DLD devices with circular post arrays indicating that an effective diameter of a deformable particle may change with the flow rate or equivalently that the deformation of such particles depends on the stresses and profile of microfluidic flow. In this study, we employ coarse-grained methods and two-dimensional (2D) models to simulate the motion of rigid spherical particles and deformable RBCs in DLD devices with different post geometries. Since such DLD geometries are at the microscale, simulation techniques on atomic or molecular levels become unfeasible. Therefore, we employ a coarse-grained hydrodynamics method at the mesoscale called dissipative particle dynamics,[25,26] allowing us to access much longer length and times scales through a coarse fluid representation. The models for suspended particles are also on a much coarser level than a representation on the molecular scale. Coarse-grained simulation approaches are ideally suited for such an investigation, because they not only allow to reach the required length- and time scales but also make it possible to abstract from atomistic and molecular detail, which is irrelevant for the design of devices. Another simplification is the use of 2D simulations, which needs to be exercised with caution, since fluid flow and the motion and deformation of soft particles in microfluidics is inherently three-dimensional (3D). There are several simulation studies, such as motion of RBCs in microchannels[15,27] and the margination of white blood cells in blood flow,[28–30] which have shown that 2D and 3D simulations lead to qualitatively consistent results. This supports the idea that 2D models should also capture the essential physics of particle separation in DLDs and provide valuable insights. The main advantage of 2D simulations in comparison to 3D models is a comparatively low computational cost, which allows for systematic exploration of many relevant parameters in DLDs.

As an initial proof of the method, we compare simulation results for hard spherical particles in a circular-post array with experimental results. We demonstrate by this comparison that for this case, 2D simulations provide near quantitative results due to the symmetry of spherical particles. This is not an obvious result, since the flow field near a spherical particle in 3D is of course not the same as that near a circular particle in 2D. Then, the effect of post shape on the transit modes of rigid spherical particles is examined including diamond, square, and triangular posts. The simulation results confirm that a deterministic picture of the three modes described above also holds for the DLD devices with non-circular post shapes. However, the transition from displacement to zigzag mode may shift for different post geometries in comparison with the circular ones. To describe this transition, an empirical formula (Eq. (8)) by Davis[39] is generalized in order to accommodate the results for other post shapes. Subsequently, similar sets of simulations are performed for RBCs to investigate the effects of deformability and orientation in relation to the critical diameters for hard spheres. Simulations show that the transit of RBCs through a DLD device strongly depends on their deformation and dynamics in flow, in agreement with previous simulation studies.[22–24] Thus, the simple description of particle transit based on the characteristic critical size becomes invalid. The predictions for particle transit must instead depend on a number of conditions including device geometry and structure, flow rate, and mechanical properties of the particle. Even though these

effects significantly complicate such systems, they also lead to new opportunities in particle sorting and detection. Hence, we expect that new sorting designs, which use particle shape, deformability, and other intrinsic properties as a target, can be developed.

II. METHODS AND MODELS

To model fluid flow within a microfluidic device, we employ the dissipative particle dynamics (DPD) method,[25,26] which is a mesoscopic particle-based hydrodynamics approach. Suspended particles are represented by a bead-spring model using a ring-like structure. The particles are coupled to fluid flow by friction forces, which are naturally part of DPD.

A. Simulation method

DPD[25,26] is a mesoscopic simulation technique which has been successfully applied to study various complex fluids.[31,32] In DPD, a simulated system consists of a collection of N fluid particles with mass m_i, position $\boldsymbol{r}_i$, and velocity $\boldsymbol{v}_i$ and each individual particle represents a cluster of atoms or molecules. The dynamics of DPD particles is governed by Newton's second law of motion as follows:

$$\begin{aligned} d\boldsymbol{r}_i &= \boldsymbol{v}_i dt, \\ d\boldsymbol{v}_i &= \frac{1}{m_i}\sum_{j\neq i}\boldsymbol{F}_{ij}dt = \frac{1}{m_i}\sum_{j\neq i}(\boldsymbol{F}^C_{ij}+\boldsymbol{F}^D_{ij}+\boldsymbol{F}^R_{ij})dt, \end{aligned} \tag{1}$$

where $\boldsymbol{F}_{ij}$ is the total force acting between two particles i and j within a selected cutoff radius r_c. The total force is a sum of three pairwise forces: conservative ($\boldsymbol{F}^C_{ij}$), dissipative ($\boldsymbol{F}^D_{ij}$), and random ($\boldsymbol{F}^R_{ij}$) forces given by

$$\begin{aligned} \boldsymbol{F}^C_{ij} &= a_{ij}(1-r_{ij}/r_c)\hat{\boldsymbol{r}}_{ij}, \\ \boldsymbol{F}^D_{ij} &= -\gamma_{ij}\omega^D(r_{ij})(\boldsymbol{v}_{ij}\cdot\hat{\boldsymbol{r}}_{ij})\hat{\boldsymbol{r}}_{ij}, \\ \boldsymbol{F}^R_{ij} &= \sigma_{ij}\omega^R(r_{ij})\xi_{ij}dt^{-1/2}\hat{\boldsymbol{r}}_{ij}, \end{aligned} \tag{2}$$

where $\boldsymbol{v}_{ij}=\boldsymbol{v}_i-\boldsymbol{v}_j$, $\boldsymbol{r}_{ij}=\boldsymbol{r}_i-\boldsymbol{r}_j$, $r_{ij}=|\boldsymbol{r}_{ij}|$, and $\hat{\boldsymbol{r}}_{ij}=\boldsymbol{r}_{ij}/|\boldsymbol{r}_{ij}|$. The coefficients a_{ij}, γ_{ij}, and σ_{ij} characterize the strength of the conservative, dissipative, and random forces, respectively. Both $\omega^D(r_{ij})$ and $\omega^R(r_{ij})$ are distance-dependent weight functions. ξ_{ij} is a random number generated from a Gaussian distribution with zero mean and unit variance.

The dissipative and random forces act together as a thermostat to maintain an equilibrium temperature T and generate a correct equilibrium Gibbs-Boltzmann distribution. Therefore, they must satisfy the fluctuation-dissipation theorem[26] given by the conditions $\omega^D(r_{ij})=[\omega^R(r_{ij})]^2$ and $\sigma^2=2\gamma k_BT$. In the original DPD method, the weight function has been chosen as $\omega^R(r_{ij})=(1-r_{ij}/r_c)^k$, with $k=1$, while different choices for this exponent have been made in other studies[33,34] in order to increase the viscosity of the DPD fluid. The viscosity of a DPD fluid has been calculated using a reverse-Poiseuille flow setup,[35] where the flow in two halves of a periodic computational domain is driven in opposite directions. Equations of motion (1) are integrated using the velocity-Verlet algorithm.[36] Table I presents the DPD parameters used in our simulations.

TABLE I. DPD fluid parameters used in simulations. Mass and length for DPD fluid are measured in units of the fluid particle mass m and the cutoff radius r_c. n is the fluid's number density, a is the repulsive-force coefficient, γ is the dissipative-force coefficient, k is the weight-function exponent, and η is the fluid's dynamic viscosity. In all simulations, we have set $m=1$, $r_c=1.5$, and the thermal energy $k_BT=1$.

nr_c^2	ar_c/k_BT	$\gamma r_c/\sqrt{mk_BT}$	k	$\eta r_c^2/\sqrt{mk_BT}$
11.25	60	30	0.15	325

B. Suspended particles

We employ $2D$ simulations, where both rigid circular particles and RBCs are modeled as closed bead-spring chains with N_v particles connected by $N_s=N_v$ springs. The spring potential is given by

$$V_{sp}=\sum_{j=1}^{N_s}\left[\frac{k_BTl_m}{4p}\frac{(3x_j^2-2x_j^3)}{(1-x_j)}+\frac{k_p}{l_j}\right], \tag{3}$$

where l_j is the length of the spring j, l_m is the maximum spring extension, $x_j=l_j/l_m\in(0,1)$, p is the persistence length, k_BT is the energy unit, and k_p is the spring constant. A balance between the two force terms in Eq. (3) leads to a nonzero equilibrium spring length l_0. Alternatively, a selected l_0 defines a ratio between the coefficients p and k_p, while their absolute values determine the spring strength such that the Young's modulus of this spring is given by

$$Y=l_0\left(\frac{\partial^2V_{sp}}{\partial l^2}\right)|_{l=l_0}=\frac{k_BTx_0}{p}\left(\frac{1}{2(1-x_0)^3}+1\right)+\frac{2k_p}{l_0^2}, \tag{4}$$

where $x_0=l_0/l_m$.

To incorporate membrane bending rigidity, a bending energy[29] is applied as

$$V_{bend}=\sum_{j=1}^{N_s}k_b[1-\cos(\theta_j)], \tag{5}$$

where k_b is the bending constant and θ_j is the instantaneous angle between two adjacent springs sharing the common vertex j. Furthermore, an area constraint is imposed for each ring polymer given by

$$V_{area}=\frac{k_a}{2}(A-A_0)^2, \tag{6}$$

where k_a is the area constraint coefficient, A_0 is the desired enclosed area, and A is the instantaneous area.

The combination of the targeted area A_0, the contour length $L_0=N_sl_0$, and the bending constant k_b controls the shape and rigidity of cells and circular particles. A circular particle is characterized by a diameter $D_{SP}=L_0/\pi$. To make a circular particle nearly rigid, its targeted area A_0 has been set to 4% larger than the area of a circle with the contour length L_0. This choice results in a considerable membrane tension due to the competition of spring and area-constraint forces making the particle virtually non-deformable. A RBC is characterized by the effective diameter $D_{RBC}=L_0/\pi$ and the reduced area $A^*=4A_0/(\pi D_{RBC}^2)=0.46$ leading to a typical biconcave shape. The other particle parameters used in simulations are given in Table II.

TABLE II. Model parameters for suspended particles. N_v is the number of vertices, l_m is the maximum spring extension, l_0 is the equilibrium spring length, and D is a characteristic particle diameter which denotes D_{SP} or D_{RBC}. κ is the macroscopic bending rigidity and $\kappa = k_b l_0$ with k_b being the bending constant, Y is the Young's modulus, A_0 is the targeted area, and k_a is the area constraint coefficient.

	N_v	l_m/l_0	$\kappa/(k_BTl_0)$	YD/k_BT	A_0/D^2	k_aD^2/k_BT
Circles	30…60	2.2	500	180 000	$1.04\pi/4$	97 000
RBCs	50	2.2	50	9 000	0.36	37 430

C. Coupling between fluid and suspended particles

Coupling between the fluid flow and suspended particles is achieved through viscous friction using the dissipative (F^D) and random (F^R) DPD forces. The repulsive-force coefficient for the coupling interactions is set to zero. The strength γ of the dissipative force is computed such that no-slip BCs are enforced. The derivation of γ is based on the idealized case of linear shear flow over a part of a membrane with the length L. In a continuum description, the total shear force exerted by the fluid on the length L is equal to $L\eta\dot{\gamma}$, where $\dot{\gamma}$ is the local wall shear-rate. The same fluid force has to be also transmitted onto a discrete surface structure having N_L vertices within the length L. The force on a single vertex exerted by the fluid can be found as $F_A = \int_{A_h} ng(r)F^D dA$, where n is the fluid number density, $g(r)$ is the radial distribution function of fluid particles with respect to the membrane particles, and A_h is the half circle area of fluid above the membrane. The total shear force on the length L is equal to $N_L F_A$. The equality $N_L F_A = L\eta\dot{\gamma}$ results in an expression of the dissipative force coefficient in terms of the fluid density and viscosity, wall density N_L/L, and r_c. Under the assumption of linear shear flow, the shear rate $\dot{\gamma}$ cancels out. This formulation results in satisfaction of the no-slip BCs for the linear shear flow over a flat surface; however, it also serves as an excellent approximation for no-slip at the membrane surface.[37] Since the conservative interactions are turned off, the radial distribution function is structureless such that $g(r) = 1$.

D. Simulation setup

A DLD device is simulated using a single obstacle and suspended particle within the computational domain. This is possible due to periodic repetition of the device geometry as illustrated in Fig. 1(b). Thus, we employ periodic boundary conditions (BCs) both in the flow and row-shift directions denoted by x and y, respectively. However, for the BCs in x, a shift in the y direction is necessary in order to mimic the shift between two consecutive rows of posts. Here, such a shift is introduced for every boundary-crossing interaction or event.

Several obstacle geometries are considered, including a circle, a square, a diamond, and a triangle depicted in Fig. 1(a). Figure 1(a) also defines the center-of-mass for these post geometries and their sizes denoted by W and H, $W = H = 15$ μm in our simulations. No-slip wall BCs are modeled by a layer of frozen particles with a thickness of r_c whose equilibrium structure characterized by the radial distribution function is the same as that of the suspending fluid. This minimizes problems with near-wall particle interactions (e.g., significant fluid-density fluctuations near the wall) which may occur due to an improper distribution of conservative forces. To prevent wall penetration, fluid particles as well as suspended structures are subject to reflection at the fluid-solid interface. Bounce-back reflections are employed, since they provide a better approximation for the no-slip BCs in comparison to specular reflection of particles. To ensure that no-slip BCs are strictly satisfied, we also add a tangential adaptive shear force[38] which acts on the fluid particles in a near-wall layer of thickness r_c.

The flow in the x direction is driven by a force applied to each fluid particle. The force value can be tuned to obtain a flow rate of interest. The shift between consecutive rows results in a nonzero net flow in the y direction. However, real DLD devices have a limited width and the net flow in the y direction is prohibited by its side walls. To mimic this situation, we have also introduced a force in y direction which can adapt to follow the condition of no net-flow in the y direction. Thus, the force in x direction controls the flow rate, while the force in y direction ensures no net flow in y direction.

In order to relate simulation and physical parameters, we need to define a time scale. For the case of rigid particles, a time scale can be defined through the fluid viscosity. However, in this case under the assumption of Stokes flow, different flow rates lead to flow profiles which can be scaled to each other due to the linearity of the Stokes equation. Thus, the time scaling here is not crucial. In case of flowing RBCs, different flow rates would result in different cell deformations and need to be looked at separately. In order to define a time scale in this case, we use a characteristic RBC relaxation time defined as

$$\tau = \frac{\eta D_{RBC}^3}{\kappa}. \tag{7}$$

Using this time scale we can, for instance, relate simulation and physical flow rates. Typical values for healthy RBCs are $D_{RBC} = 6.1$ μm, $\eta = 1.2 \times 10^{-3}$ Pa s is the viscosity of blood plasma, and κ lies within the range of $50–70k_BT$ for the physiological temperature $T = 37$ °C.

III. RESULTS AND DISCUSSION

A. Separation of rigid spherical particles in circular post arrays

The dynamics of rigid spherical particles flowing in conventional circular-post arrays is rather well understood. Two transport modes, zigzag and displacement, were experimentally observed depending on particle size.[7] To estimate the critical particle size D_c for the transition between

the two transport modes, an empirical formula has been suggested based on results of a systematic experimental study[39] by varying the gap size and particle diameter and assuming a parabolic flow profile between two neighboring posts. The proposed formula is given by[39]

$$D_c = 1.4G\varepsilon^{0.48}, \tag{8}$$

where ε is the row-shift fraction defined as $\varepsilon = \Delta\lambda/\lambda$. In the current study, 2D mesoscopic simulations are employed to investigate the effect of post shapes on the separation of spherical and non-spherical particles. Before the exploration of a more complex geometry and structure of posts and particles, careful testing and validation of the simulated system are essential. For this purpose, we have studied the separation of rigid spherical particles with 7 different diameters ($D_{SP} \in [2.78, 5.59]$ μm) in circular post arrays by varying the row shift. A detailed comparison between our simulation results and the predictions obtained from the empirical formula, Eq. (8), is performed in order to assess the quality of simulation predictions.

Figure 2(a) presents typical trajectories of a spherical particle with $D_{SP} = 5.12$ μm in circular post arrays at different row shifts. It is clear that the particle moves according to the

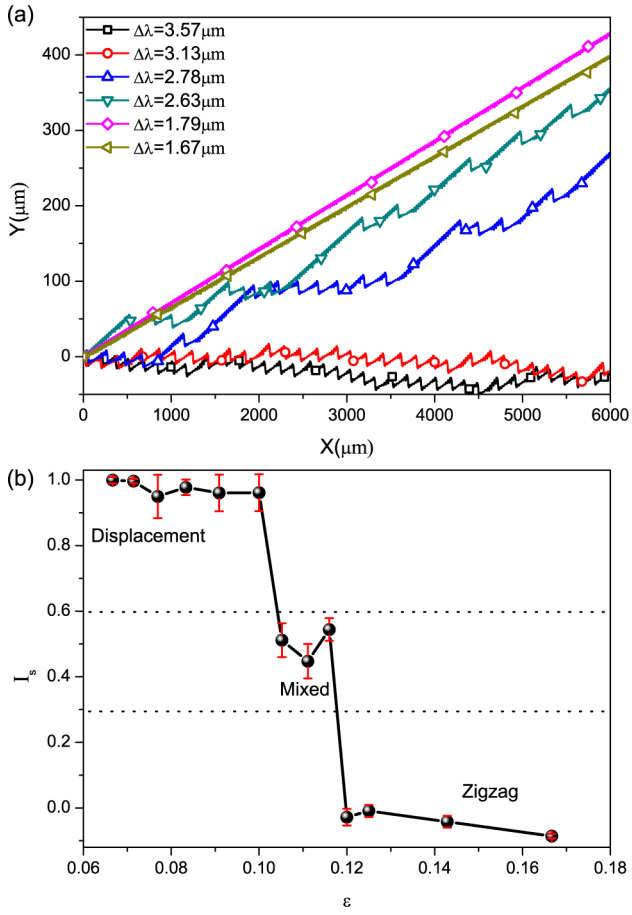

FIG. 2. (a) Typical trajectories of a 2D rigid spherical particle with $D_{SP} = 5.12$ μm in the conventional circular post arrays at different row shifts $\Delta\lambda$. (b) The separation index I_s, which is defined as the ratio of the lateral displacement of particles per post to the row shift, for the corresponding particle sorting as a function of the row-shift fraction. Error bars are indicated for all data points.

displacement mode at low row shifts ($\Delta\lambda \lesssim 2.5$ μm) and follows the zigzag mode for larger row shifts ($\Delta\lambda \gtrsim 3.0$ μm). However, it is interesting to note that at some intermediate values of the row shift, particle trajectories exhibit an irregular alternation between displacement and zigzag motions, which will be referred to as "mixed mode" subsequently. Similar motion has been also observed in experiments[2,9,10,40] and previous simulations.[9,10] Huang *et al.*[2] suggested that this behavior can be attributed to Brownian motion (or diffusion) of particles between different streamlines. We have performed several simulations using a larger ambient temperature in DPD (approximately by a factor of two), which leads to an increased diffusivity of suspended particles. These results qualitatively indicate that the mixed-mode region becomes slightly wider in the row-shift fraction. This is not very surprising, since as the displacement-to-zigzag transition is approached, particle diffusion might make a difference, leading to a widening of the transition region (or the mixed-mode region). In contrast, Kulrattanarak *et al.*[9,10] have proposed that the occurrence of mixed mode is due to the asymmetric flowline distribution between posts in certain DLD devices with $G_x/G_y \leq 3$ and $D_{post}/G_y > 0.4$, where G_x and G_y are the post gap sizes in x and y directions, respectively. The geometry of our simulated DLD array is in this range with $G_x = G_y = G$ and $D_{post}/G_y = 1.5$. It is important to note that this proposition is based on fluid-flow simulations with a point-like tracer particle; however, for a finite-size particle (e.g., with a diameter comparable to the gap size), the disturbance field around the particle has to be taken into account and may significantly contribute to the particle motion within a DLD array. Furthermore, our simulation method naturally includes thermal fluctuations, and therefore, particle diffusion cannot be excluded as a potential contribution to the mixed mode.

To quantitatively characterize the motion of particles within DLD, we introduce a dimensionless parameter called "separation index" I_s, defined as the ratio of the lateral displacement of particles per post to the row shift. For the ideal displacement mode, I_s should be close to unity, since particles are forced to displace laterally along the shift gradient of the post array. For the ideal zigzag mode, I_s should be close to zero as the particles move with the flow without a significant net lateral displacement. The concept behind this parameter is similar to the "migration angle"[2,9,10] or "separation index"[41] used in experiments. Due to the existence of mixed mode, the value of I_s in our simulated trajectories is not just 1 or 0. As illustrated in Fig. 2(b), there exist a small plateau with intermediate values of I_s and some variation, indicating the mixed mode. Moreover, the value of I_s is found to remain in the range of 0.3–0.6 regardless of the initial position of a particle and simulation time, which further confirms the existence of the mixed mode. Away from the mixed region, I_s quickly attains values close to 1 or 0. In view of these results, the magnitude of $I_s \in [0.3, 0.6]$ is used as a quantitative measure for the mixed mode and the transition to/from zigzag or displacement dynamics. Therefore, $I_s > 0.6$ and $I_s < 0.3$ are chosen to define the displacement and zigzag modes, respectively.

The identical strategy and analysis have been employed to assess the separation of all the seven particle diameters in

circular post arrays. The observed modes as a function of the row shift fraction (ε) and the normalized particle diameter (D_{SP}/G) are summarized in Fig. 3. It is apparent that the critical particle sizes calculated from the empirical formula of Eq. (8) approximately reside in the region of mixed mode which defines the transition from the zigzag to displacement mode. The good agreement between our simulations and experimental results of Davis[39] validates the 2D model and shows that it is able to capture the essential physical features required to correctly describe the particle separation in conventional DLD devices with circular posts. Therefore, further simulations with modifications of the post shapes and particle properties should provide reliable and valuable guidelines for the performance of different DLD devices.

B. Effect of post shapes on the separation of rigid spherical particles

Diamond, square, and triangular posts have also been studied to explore the effect of post shape on the flow behavior of rigid spherical particles within DLDs. In comparison with the circular posts, the common geometric feature of these three posts is the sharp edges of the post surfaces whose curvature, position, and symmetry all strongly affect the flow properties in post gaps. Indeed, significant changes are observed in the flow profiles for different post arrays, as depicted in Fig. 4. The plots show that the region of the largest flow velocity within the post gaps resembles elliptical, circular, cigar-like, and pear-like patterns for circular, diamond, square, and triangular posts, respectively. Moreover, it is worth mentioning that in the square-post array, there is a small region with nearly zero flow rate in the gap between adjacent columns. All these changes must alter the motion of particles through the post arrays and consequently influence the separation efficiency in DLD devices.

A collection of the different transit modes for rigid spherical particles in the diamond- and square-post arrays is shown in Fig. 5. In comparison with the behavior in circular-post arrays, the transition from the zigzag to displacement mode is shifted slightly or significantly to a higher value of the row-shift fraction ϵ in the diamond- or square-post arrays, respectively, indicating a reduction of the critical size in these devices. These simulation results are consistent with the experimental and numerical studies.[3,4,20,42] The reduced critical size can be understood intuitively on basis of the change of the flow profiles induced by the post shapes. According to the theory in Refs. 2, 7, and 39, fluid flow in the post gap can be split into several ($N = 1/\varepsilon$) streams carrying equal volumetric flow rate. The width $D_{f,1}$ of the first stream directly next to the post (see Fig. 4) is assumed to correspond to the critical particle radius for the transition from the zigzag to displacement mode. In general, $D_{f,1}$ is wider in comparison to middle streams in order to accommodate more fluid flow, since the first stream is at the wall with no-slip boundary conditions. For diamond-shaped posts, the existence of sharp edges in comparison to the smooth bending of a circular-post surface leads to a smaller $D_{f,1}$ and a smaller critical particle

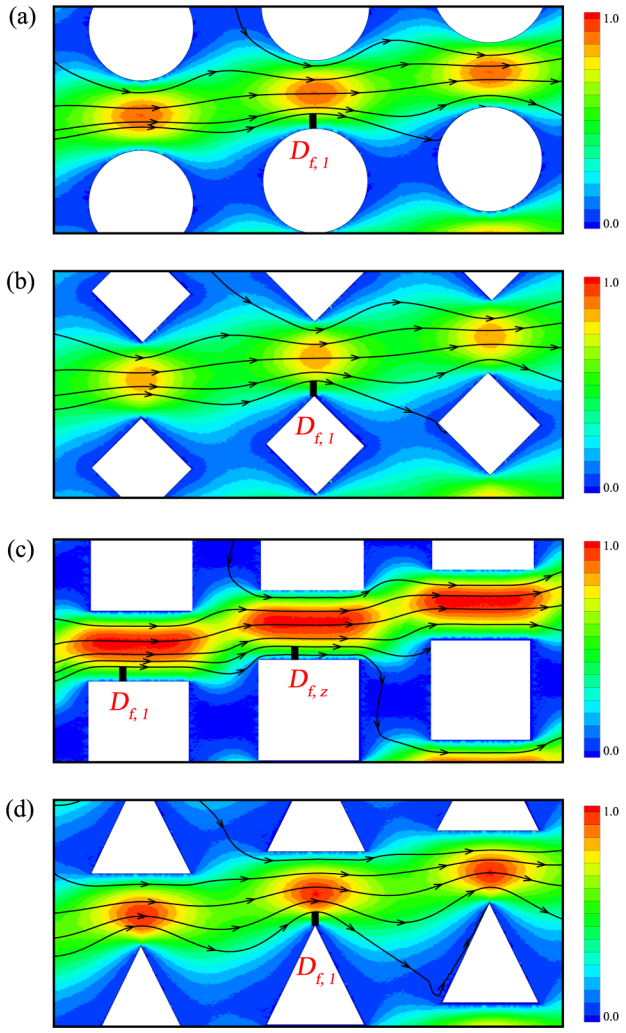

FIG. 4. Comparison of flow velocities (x component) in DLD arrays with (a) circular, (b) diamond, (c) square, and (d) triangular posts at the row shift fraction of $\varepsilon = 1/8$. All velocities in the flow direction (x axis) are normalized by the maximum value of velocity observed in the square post array. Red regions represent the high flow rate, while the dark blue regions correspond to the zero flow velocity at the boundaries with no-slip condition.

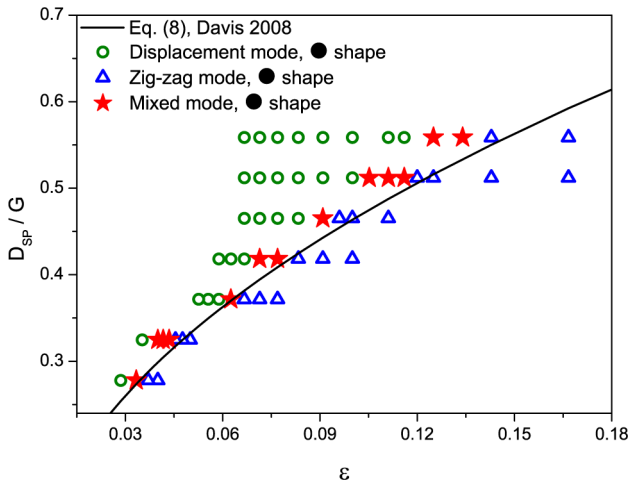

FIG. 3. Mode diagram for rigid spherical particles in circular post arrays as a function of the row shift fraction (ε) and the normalized particle diameter (D_{SP}/G). The predicted critical size from the empirical formula in Eq. (8) is drawn by the solid line.

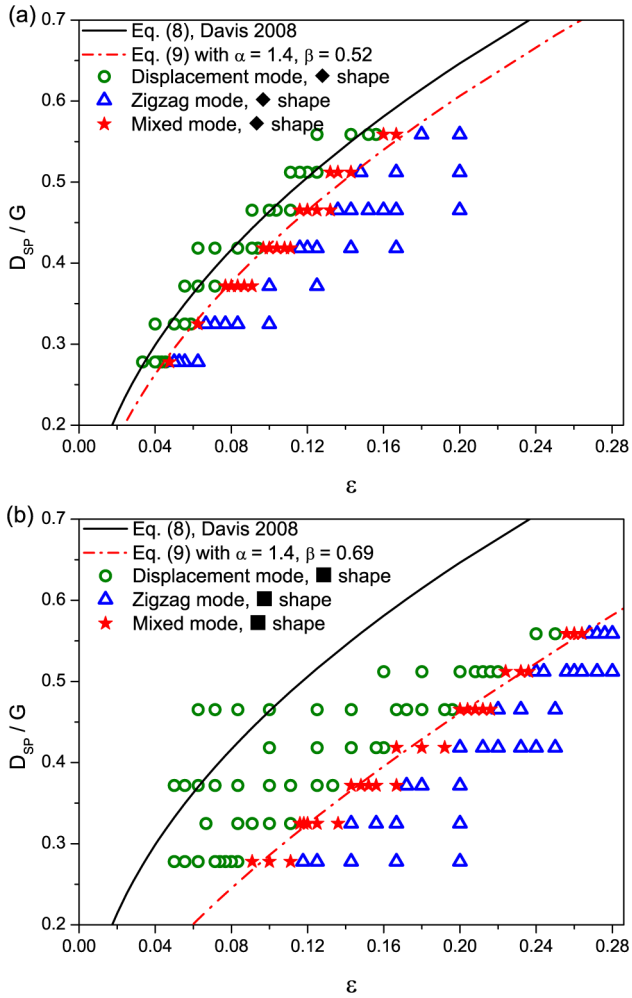

FIG. 5. Mode diagram for the rigid spherical particles in (a) diamond and (b) square post arrays as a function of the row shift fraction (ε) and the normalized particle diameter (D_{SP}/G). Critical size from the empirical formula in Eq. (8) is drawn by the solid line.

size. In contrast, the flat edges of the square-shaped post should smoothen the velocity distribution and consequently induce a larger critical size, which is in contrast to our numerical results and observations in Fig. 5. In light of this seeming contradiction, we define another stream wherein the fluid moves zigzag-like from the top to the lower channel and denote the corresponding width as $D_{f,z}$ (see Fig. 4(c)). For the circular, diamond, and triangular posts, $D_{f,z} \simeq D_{f,1}$ has been measured, while for the square posts, $D_{f,z}$ is found to be 10%–20% smaller than $D_{f,1}$ independently of the row shift. Hence, a possible reason for a strong reduction of the critical particle size in square-post arrays is that the sharp corners of square posts reside in both the inlet and outlet of the post gap and induce a small region with nearly zero flow rate in the gap between adjacent post columns. It is clear from Fig. 4 that for the circular, diamond, and triangular posts, the flow rate in the gap between adjacent post columns is significantly larger than that for the square posts. In this way, the original first stream is seriously obstructed, and therefore, a significant reduction of critical particle size is observed for square-post arrays.

Recently, Wei *et al.*[42] proposed a general formula to estimate the critical particle sizes of DLD arrays with different post shapes by introducing a shape-dependent prefactor to Eq. (8). However, this parameter is simply obtained by data fitting as a function of the row shift and a geometric parameter of the gap between adjacent post columns, which is not sufficient to describe the geometric features of post shapes. For example, their numerical studies have shown that the shape factor and the resulting formula appear to be the same for square- and I-shape posts, which is in contrast with the experimental observations.[20] Additionally, the critical particle size from their formula[42] used for square post arrays is found to significantly deviate from our predictions in most cases. In view of these differences, we propose a more general formula

$$D_c = \alpha G \varepsilon^{\beta}, \tag{9}$$

where the dimensionless parameters α and β are geometric factors determined by the shape and arrangement of posts. For the conventional circular posts, $\alpha = 1.4$ and $\beta = 0.48$ as in Eq. (8). For the diamond and square posts in Fig. 5, the best fitting curves are obtained for the parameters $\alpha = 1.4$, $\beta = 0.52$ and $\alpha = 1.4$, $\beta = 0.69$, respectively. Interestingly, the coefficient α remains essentially unaffected for circular, diamond, and square posts.

Unlike the symmetric shapes discussed above, the triangular posts break the top-bottom symmetry, see Fig. 1(a). Accordingly, an asymmetric flow profile with a skewed parabolic shape is induced through the gap, as can be seen from the pear-like pattern shown in Fig. 4(d). This feature results in *two distinct* critical particle sizes depending on the flow direction or row shift, which is not the case for the symmetric posts. Alternatively, the change in the flow direction or row shift for triangular posts is equivalent to turning the triangular posts upside down. As fluid moves forward in the triangular-post array with a positive row shift (see Fig. 1(b)), one critical particle size should be determined by the stream width adjacent to the top vertex of a triangle. However, for a reversed flow direction (from right to left) with negative row shift, another critical size should be governed by the stream width just above the flat bottom edge, and the corresponding value of the critical size can be expected to be smaller than that for the previous flow direction (from left to right). This tendency is in accordance with our simulation results as illustrated in Fig. 6(a). For positive row shift, the transition between the zigzag and displacement modes is shifted to higher values of row shifts, indicating a reduced critical particle size compared to that for circular posts. In contrast, an increased critical particle size is observed for negative row shifts. The fits in Fig. 6(a) using Eq. (9) correspond to parameters $\alpha = 1.4$, $\beta = 0.44$ and $\alpha = 1.4$, $\beta = 0.61$ for the negative and positive row shifts, respectively.

Figure 6(b) presents the separation index I_s for triangular-post arrays. The value of I_s not only characterizes the mode of particle motion but also provides the physical lateral displacement (i.e., $I_s \Delta\lambda$) of a particle per single row of posts. The value of I_s also provides guidance on the design of a DLD device. For instance, in case of the triangular-post array with $|\Delta\lambda| = 4$ μm ($\varepsilon = 0.16$) in Fig. 6(b), a smaller particle with $D_{SP} = 3.72$ μm is in the zigzag mode with $I_s \approx 0$, a particle with $D_{SP} = 4.65$ μm is in the mixed mode with $I_s \approx 0.5$, and

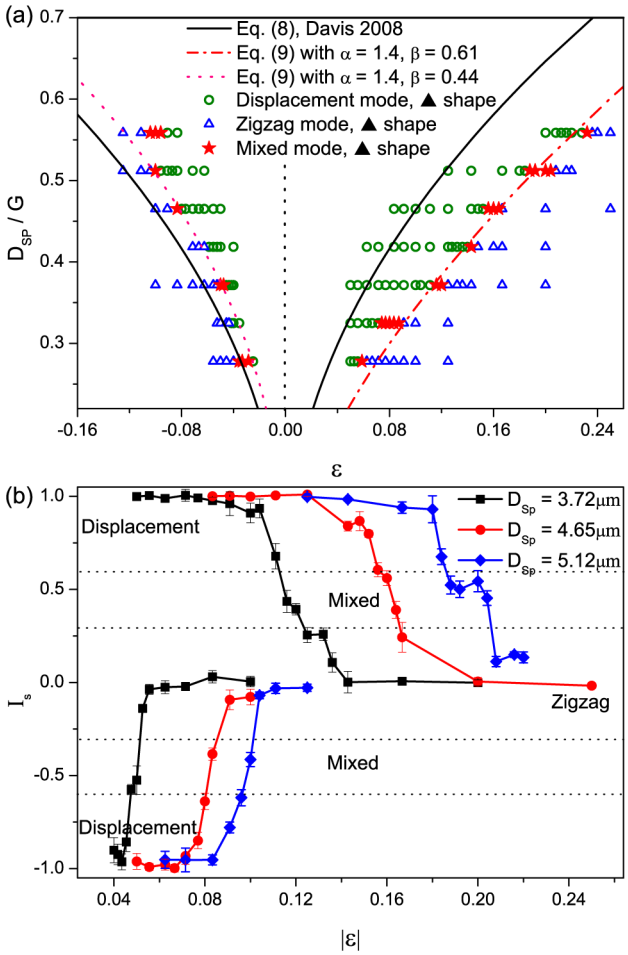

FIG. 6. (a) Mode diagram for the rigid spherical particles in triangular-post arrays as a function of the row shift fraction (ε) and the normalized particle diameter (D_{SP}/G). (b) Typical behavior of the separation index I_s as a function of the absolute value of the row-shift fraction.

a particle with $D_{SP} = 5.12$ μm is in the displacement mode with $I_s \approx 1$. Thus, the choice of such shift with $\Delta\lambda = 4$ μm within a DLD is advantageous for the separation of these three particle sizes. An analogous choice for optimal row shifts can be also made for the case of negative row displacements. An interesting observation in Fig. 6(b) is that the transition between the displacement and zigzag modes appears to be much sharper for negative in comparison to positive row shifts.

C. Motion of RBCs in different DLD arrays

So far we have focused on the motion of rigid spherical particles within DLD arrays. However, many bioparticles and cells of interest are non-spherical and deformable, and their shape and deformability are well known to largely influence their trajectories in DLD devices.[5,6,19,43] To better understand the behavior of flexible particles in flow within DLDs, we have performed a number of simulations using a 2D RBC model for various post shapes including circular-, diamond-, and square-post arrays. Since RBCs are deformable, an effective size denoted as D_{eff} is defined to characterize the transition of RBCs from the zigzag to displacement mode. Figure 7 shows the separation index for RBCs within circular, diamond, and

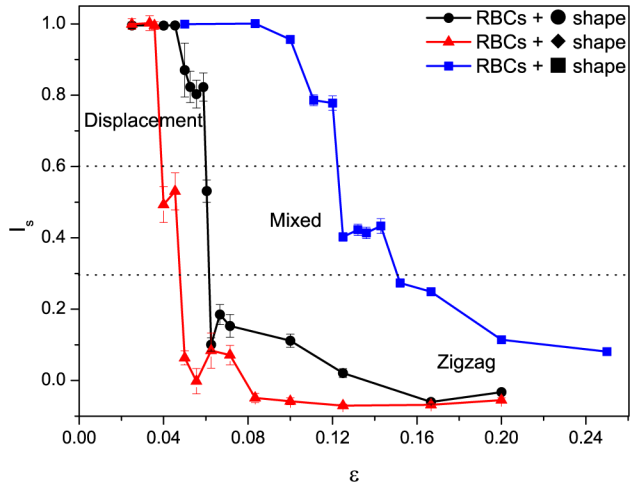

FIG. 7. Typical distributions of the separation index I_s for RBCs within circular, diamond, and square post arrays as a function of the row shift fraction.

square post arrays. We find that the transition from the zigzag to displacement mode for RBCs is at $\Delta\lambda = 1.51 \pm 0.05$ μm, 1.07 ± 0.18 μm, and 3.46 ± 0.33 μm for circular-, diamond-, and square-post arrays, respectively. According to our fits, these row-shift values correspond to $D_{eff} = 3.65 \pm 0.07$ μm, 2.65 ± 0.14 μm, and 3.50 ± 0.15 μm, respectively. These effective sizes lie between the thickness and diameter of a RBC, indicating that RBCs deform and display different dynamics in various flow fields induced by the post shapes.

Figures 8 and 9 illustrate how RBCs move and deform in the zigzag and displacement modes in different post arrays. In the zigzag mode (Fig. 8), there is usually one flipping motion in each zigzag period, which increases the effective size of RBCs and in turn facilitates the jump of RBCs from the top to the bottom stream next to the post. This process can be occasionally accomplished by a dramatic deformation, as depicted in the first zigzag motion in Fig. 8(c). After that, RBCs usually slip smoothly past the subsequent posts by slightly deforming along the geometry of a post. If $D_{eff} > 2D_{f,1}$, RBCs enter the adjacent stream and flow above the next post, resulting in the displacement motion depicted in Fig. 9. It is important to note that when $D_{eff} \gg 2D_{f,1}$ in the square-post array, the displacement motion of RBCs changes from slipping around the posts (see Figs. 8(a) and 8(b)) to avoiding any contact with the post and moving quickly with an orientation parallel to the gradient of array (Fig. 8(c)). This novel behavior is due to the cigar-like flow profile in the gap, which resembles flow in a short cylindrical microchannel. In microchannel flow, RBCs migrate away from the channel walls due to hydrodynamic interactions of RBCs with the walls, which is often referred to as *lift force*.[44–46] If $D_{eff} < 2D_{f,1}$, RBCs move along the zigzag path of the first stream. Here, the flow profile in the gap between the adjacent post columns plays an important role in deforming RBCs and consequently influences their flow path. As an example, for the case of square posts in Fig. 8(c), after slipping past the post, RBCs subside gradually from the top channel and flip into the lower channel, which is clearly different from the motions in circular- and diamond-post arrays.

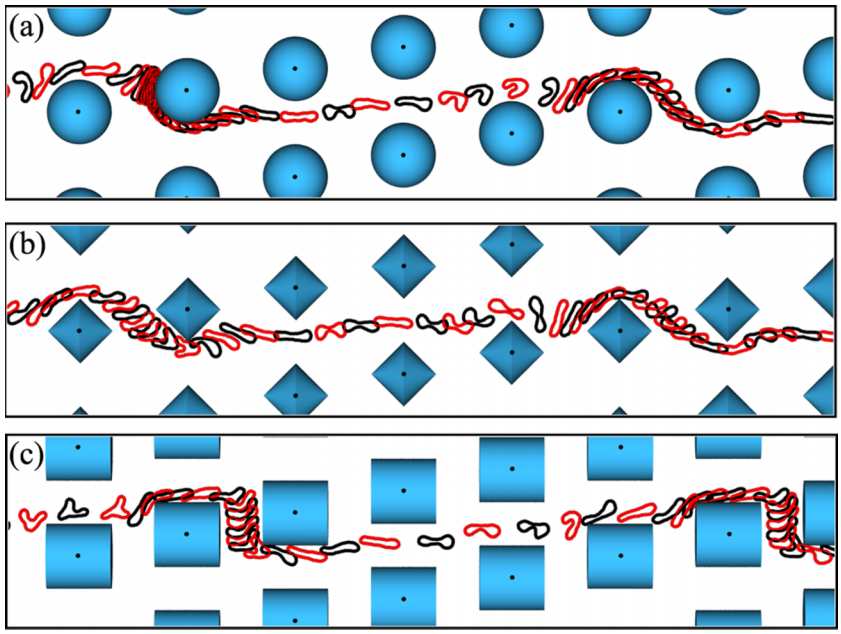

FIG. 8. Snapshots of typical zigzag trajectories of RBCs in DLD arrays with (a) circular, (b) diamond, and (c) square posts at $\Delta\lambda = 5.0\ \mu$m. The regular alternation of black and red RBCs represents sequential frames with an interval of 0.023τ.

To describe the shape and morphology change of RBCs in DLD arrays, a parameter called asphericity δ is used to measure the deviation from spherical (or circular) geometry,

$$\delta = \frac{(\lambda_1 - \lambda_2)^2}{(\lambda_1 + \lambda_2)^2}, \tag{10}$$

where λ_1 and λ_2 are the square root of two non-zero eigenvalues of the squared radius-of-gyration tensor. The value of δ varies from 0 to 1, corresponding to a perfect circle and a strongly elongated object, respectively. For a biconcave 2D RBC shape in equilibrium, the asphericity is equal to $\delta \approx 0.29$. Following this definition, Fig. 10 presents the morphology change of RBCs under different conditions in terms of a probability density. It is apparent that with the transition from the displacement to zigzag mode with increasing row shift, RBCs are subject to more deformation in both circular- and square-post arrays, as indicated by the higher probability for lower asphericities shown in Figs. 10(a) and 10(c). However, RBCs display significant deformation in both zigzag and displacement modes, which is also confirmed by the flipping motion in Figs. 8(b) and 9(b).

In view of these observations, a zigzag period can be divided into two stages: (i) particle motion across the gap toward the first stream above the post and (ii) flowing along the zigzag path of the stream. For rigid spherical particles, it is a straightforward and deterministic process based on particle size. For soft particles or cells however, it can be very complicated, since the deformation and motion of particles are highly sensitive to the flow field within the post array. This also indicates that the flow rate in a DLD

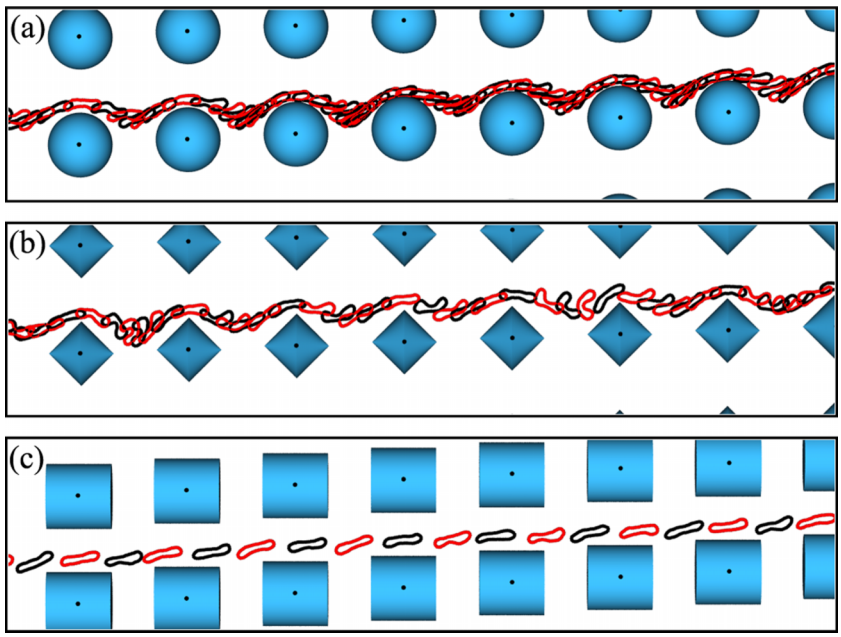

FIG. 9. Snapshots of typical displacement trajectories of RBCs in DLD arrays with (a) circular posts at $\Delta\lambda = 1.25\ \mu$m, (b) diamond posts at $\Delta\lambda = 1\ \mu$m, and (c) square posts at $\Delta\lambda = 1.25\ \mu$m. The regular alternation of black and red RBCs corresponds to sequential frames with an interval of 0.023τ.

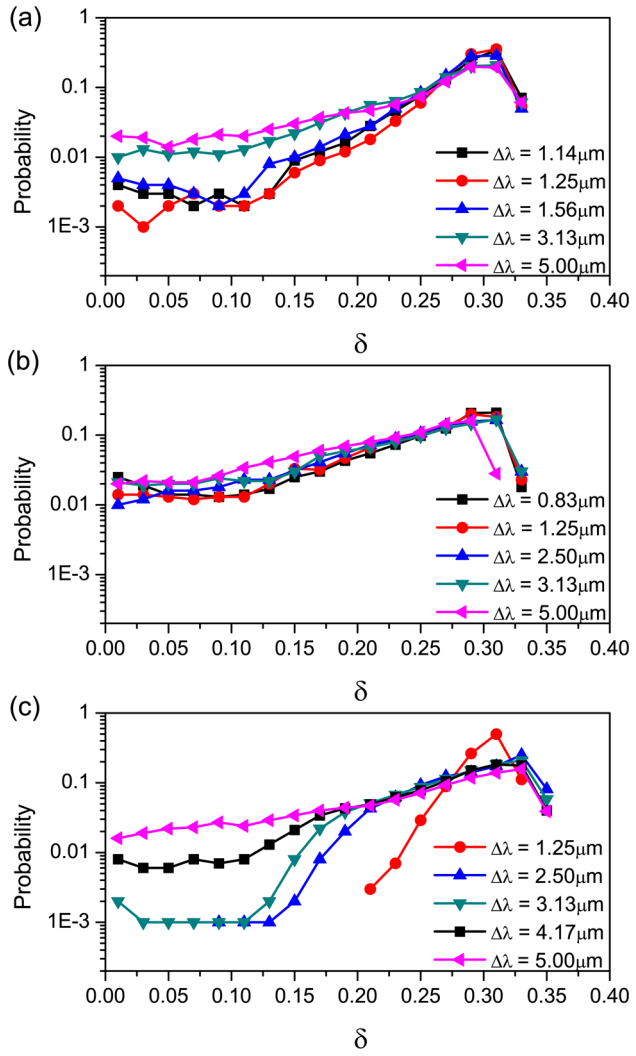

FIG. 10. Distributions of the asphericity (δ) of RBCs in DLD arrays with (a) circular, (b) diamond, and (c) square posts for various row shifts.

device becomes an additional parameter to consider for the separation of soft particles and cells. The effect of flow rate on the RBC motion within a DLD device with circular posts has been already investigated experimentally,[19] showing a strong dependence. In another experimental study, it has been found that a rotational motion of a non-isotropic particle induced by I-shape posts might be advantageous for particle sorting.[20] A similar rotational motion has been also observed in our study for RBCs in particular for diamond- and square-shaped posts. As a conclusion, the notion of a single critical size for particle separation, as suggested for the rigid spherical particles, is likely to be an oversimplified concept when applied to non-isotropic, deformable particles and cells. Deformable particles and cells clearly show very rich dynamics in DLD devices, whose underling mechanisms still need to be further explored in order to reach the understanding required for a rational design of DLD devices for sorting.

IV. SUMMARY AND CONCLUSIONS

We have presented a systematic study of particle motion within DLD arrays using a coarse-grained mesoscopic modeling approach in two spatial dimensions. Several obstacle geometries including circular, diamond, square, and triangular posts and particle sizes were considered. The simulation results for rigid spherical particles in circular-post arrays are found to be in a very good agreement with the available experimental data. The dynamics of spherical particles can be divided into the three major modes: displacement, mixed, and zigzag. The displacement mode is characterized by the motion where a particle simply follows the gradient of row shift within a device with a separation index close to unity. The zigzag mode corresponds to the particle motion with nearly zero lateral displacement within the device, which can be identified by a nearly zero separation index. The mixed mode results in an intermediate state with alternating displacement and zigzag sections and can be characterized by the separation index $I_s \in [0.3, 0.6]$. The transition from the displacement to zigzag mode in circular-post arrays is well captured by an empirical formula (Eq. (8)), which defines a critical particle size.

Simulations of diamond-, square-, and triangular-post arrays display significant differences in particle critical size in comparison with the circular-post devices. The flow field strongly depends on the geometry of a device and consequently modifies particle trajectories in the corresponding post arrays. However, the behavior of a rigid spherical particle in these devices can still be well described by the three characteristic modes, and the transition from the displacement to the zigzag mode is well captured by a generalized empirical formula (Eq. (9)) with two fitting parameters. The possibility of a unified empirical description for the transition indicates that qualitatively, the same flow mechanisms are of importance in such devices, and all of them can be potentially used for the sorting of rigid spherical particles with different sizes. However, the flow details also matter when fine tuning becomes important and some geometries might be preferable depending on the problem of interest.

Finally, the flow behavior of deformable particles such as RBCs has been investigated for different post geometries. The simulations have shown that RBCs experience strong deformations due to fluid flow, which determine their corresponding mode of motion. In comparison to rigid spherical particles, the transition from the displacement to the zigzag mode becomes very broad with a significant part devoted to the mixed mode. Also, the dynamics of RBCs (e.g., tumbling) in flow plays a significant role in determining their traversal trajectory through a DLD device. Both dynamics and deformation strongly depend on the device geometry, since it is governed by local flow fields. In addition, it is expected that different flow rates within a device should lead to distinct behaviors of RBCs, making this an important parameter for consideration. These results indicate that a simplified description with a single critical size becomes invalid in case of non-isotropic and deformable particles and/or cells. The behavior of deformable particles in DLD devices is much richer in comparison with the rigid spherical particles, which not only brings additional complications but also provides new opportunities. Thus, it is plausible to expect that non-isotropic and deformable particles can be sorted based on their deformability, geometry, and potentially other intrinsic

properties. We expect that this research direction will receive considerable attention in the near future.

ACKNOWLEDGMENTS

We would like to thank Stefan H. Holm, Jason P. Beech, and Jonas O. Tegenfeldt (Lund University, Sweden) for stimulating discussions. We acknowledge the FP7-PEOPLE-2013-ITN LAPASO "Label-free particle sorting" for financial support. Dmitry A. Fedosov acknowledges funding by the Alexander von Humboldt Foundation. We also gratefully acknowledge a CPU time grant by the Jülich Supercomputing Center.

[1]J. McGrath, M. Jimenez, and H. Bridle, Lab Chip **14**, 4139 (2014).
[2]L. R. Huang, E. C. Cox, R. H. Austin, and J. C. Sturm, Science **304**, 987 (2004).
[3]K. Loutherback *et al.*, Microfluid. Nanofluid. **9**, 1143 (2010).
[4]K. Loutherback, J. Puchalla, R. H. Austin, and J. C. Sturm, Phys. Rev. Lett. **102**, 045301 (2009).
[5]S. H. Holm, J. P. Beech, M. P. Barrett, and J. O. Tegenfeldt, Lab Chip **11**, 1326 (2011).
[6]J. A. Davis *et al.*, Proc. Natl. Acad. Sci. U. S. A. **103**, 14779 (2006).
[7]D. W. Inglis, J. A. Davis, R. H. Austin, and J. C. Sturm, Lab Chip **6**, 655 (2006).
[8]H. N. Joensson, M. Uhlen, and H. Andersson-Svahn, Lab Chip **11**, 1305 (2011).
[9]T. Kulrattanarak *et al.*, J. Colloid Interface Sci. **354**, 7 (2011).
[10]T. Kulrattanarak, R. G. M. van der Sman, C. G. P. H. Schroën, and R. M. Boom, Microfluid. Nanofluid. **10**, 843 (2011).
[11]H. Noguchi, G. Gompper, L. Schmid, A. Wixforth, and T. Franke, Europhys. Lett. **89**, 28002 (2010).
[12]J. L. McWhirter, H. Noguchi, and G. Gompper, Proc. Natl. Acad. Sci. U. S. A. **106**, 6039 (2009).
[13]G. Tomaiuolo, M. Simeone, V. Martinelli, B. Rotoli, and S. Guido, Soft Matter **5**, 3736 (2009).
[14]B. Kaoui, G. Biros, and C. Misbah, Phys. Rev. Lett. **103**, 188101 (2009).
[15]D. A. Fedosov, M. Peltomäki, and G. Gompper, Soft Matter **10**, 4258 (2014).
[16]A. Walter, H. Rehage, and H. Leonhard, Colloids Surf., A **183-185**, 123 (2001).
[17]S. Kessler, R. Finken, and U. Seifert, J. Fluid Mech. **605**, 207 (2008).
[18]P. M. Vlahovska, Y.-N. Young, G. Danker, and C. Misbah, J. Fluid Mech. **678**, 221 (2011).
[19]J. P. Beech, S. H. Holm, K. Adolfsson, and J. O. Tegenfeldt, Lab Chip **12**, 1048 (2012).
[20]K. K. Zeming, S. Ranjan, and Y. Zhang, Nat. Commun. **4**, 1625 (2013).
[21]M. Al-Fandi, M. Al-Rousan, M. A. K. Jaradat, and L. Al-Ebbini, Rob. Comput.-Integr. Manuf. **27**, 237 (2011).
[22]R. Quek, D. V. Le, and K.-H. Chiam, Phys. Rev. E **83**, 056301 (2011).
[23]L. Zhu, C. Rorai, D. Mitra, and L. Brandt, Soft Matter **10**, 7705 (2014).
[24]T. Krüger, D. Holmes, and P. V. Coveney, Biomicrofluidics **8**, 054114 (2014).
[25]P. J. Hoogerbrugge and J. M. V. A. Koelman, Europhys. Lett. **19**, 155 (1992).
[26]P. Español and P. Warren, Europhys. Lett. **30**, 191 (1995).
[27]B. Kaoui *et al.*, Phys. Rev. E **84**, 041906 (2011).
[28]J. B. Freund, Phys. Fluids **19**, 023301 (2007).
[29]D. A. Fedosov, J. Fornleitner, and G. Gompper, Phys. Rev. Lett. **108**, 028104 (2012).
[30]D. A. Fedosov and G. Gompper, Soft Matter **10**, 2961 (2014).
[31]I. V. Pivkin, B. Caswell, and G. E. Karniadakis, "Dissipative particle dynamics," in *Reviews in Computational Chemistry*, edited by K. B. Lipkowitz (John Wiley & Sons, Inc., Hoboken, NJ, USA, 2011), Vol. 27, pp. 85–110.
[32]D. A. Fedosov, H. Noguchi, and G. Gompper, Biomech. Model. Mechanobiol. **13**, 239 (2014).
[33]X. Fan, N. Phan-Thien, S. Chen, X. Wu, and T. Y. Ng, Phys. Fluids **18**, 063102 (2006).
[34]D. A. Fedosov, G. E. Karniadakis, and B. Caswell, J. Chem. Phys. **128**, 144903 (2008).
[35]J. A. Backer, C. P. Lowe, H. C. J. Hoefsloot, and P. D. Iedema, J. Chem. Phys. **122**, 154503 (2005).
[36]M. P. Allen and D. J. Tildesley, *Computer Simulation of Liquids* (Clarendon Press, New York, 1991).
[37]D. A. Fedosov, B. Caswell, and G. E. Karniadakis, Biophys. J. **98**, 2215 (2010).
[38]D. A. Fedosov and G. E. Karniadakis, J. Comput. Phys. **228**, 1157 (2009).
[39]J. A. Davis, "Microfluidic separation of blood components through deterministic lateral displacement," Ph.D. thesis, Princeton University, USA, 2008.
[40]B. R. Long *et al.*, Phys. Rev. E **78**, 046304 (2008).
[41]S. Ranjan, K. K. Zeming, R. Jureen, D. Fisher, and Y. Zhang, Lab Chip **14**, 4250 (2014).
[42]J. Wei *et al.*, IEEE Trans. NanoBiosci. **14**, 660 (2015).
[43]K. Loutherback *et al.*, AIP Adv. **2**, 042107 (2012).
[44]I. Cantat and C. Misbah, Phys. Rev. Lett. **83**, 880 (1999).
[45]M. Abkarian, C. Lartigue, and A. Viallat, Phys. Rev. Lett. **88**, 068103 (2002).
[46]S. Messlinger, B. Schmidt, H. Noguchi, and G. Gompper, Phys. Rev. E **80**, 011901 (2009).